Research Article

Nano Research
2023, 16(7): 10634–10643

ISSN 1998-0124 CN 11-5974/O4
https://doi.org/10.1007/s12274-023-5613-2

Controllable construction of $La_2Li_{0.5}Co_{0.5}O_4$ multifunctional "armor" to stabilize Li-rich layered oxide cathode for high-performance lithium-ion batteries

Xiaoyang Deng[1,§], Mi Li[1,§], Zizai Ma[2,3], and Xiaoguang Wang[1,2] (✉)

[1] *Institute of New Carbon Materials, College of Materials Science and Engineering, Taiyuan University of Technology, Taiyuan 030024, China*
[2] *Shanxi Key Laboratory of Gas Energy Efficient and Clean Utilization, Taiyuan 030024, China*
[3] *College of Chemistry, Taiyuan University of Technology, Taiyuan 030024, China*
[§] *Xiaoyang Deng and Mi Li contributed equally to this work.*

Received: 11 December 2022 / **Revised:** 23 February 2023 / **Accepted:** 23 February 2023

ABSTRACT

Lithium-rich manganese-based cathodes (LR) are valuable cathode materials for the next generation of lithium-ion batteries (LIBs) with high-energy density. However, the fast voltage/capacity decay on cycling is the major obstacle for the practical application induced by the less-than-ideal anionic redox reactions and structure distortion. Herein, in order to tackle these challenges, a perovskite-like $La_2Li_{0.5}Co_{0.5}O_4$ (LLCO) material is selected as protective surface to stabilize the $Li_{1.2}Mn_{0.54}Ni_{0.13}Co_{0.13}O_2$ (LR) substrate through wet chemical coating method. Versatile structure/phase characterizations and electrochemical tests exhibit that the LLCO can not only minish the oxygen evolution and enhance the structure stability, but also restrain the electrolyte corrosion and increase the mechanical strength of cathode materials. Moreover, the coated LLCO with high electronic/ionic conductivity dramatically accelerates the energy storage kinetic, thereby displaying the improved rate performance. Specifically, the optimized LR@LLCO sample (1LLCO) exhibits a high capacity of 250.6 mAh·g^{-1} after 100 cycles at 0.1 C and excellent capacity retention of 82.6% after 200 cycles at 2 C. This work provides a new idea for the modification of LR cathodes toward commercial high-performance LIBs.

KEYWORDS

lithium-rich manganese-based oxide, lithium-ion batteries, surface modification, electrochemical performance

1 Introduction

The booming development of smart grid and electric vehicle market has stimulated the demand for lithium-ion batteries (LIBs) with higher energy density and power density. To date, the progress of the state-of-the-art cathode materials has become the main bottleneck of the high-performance LIBs [1, 2]. Among the current commercial cathodes, lithium-rich manganese-based cathodes (LRs) are considered to be one of the most promising cathodes for building high-performance batteries, due to their high specific capacity (> 250 mAh·g^{-1} under high working voltage) and desirable cost effectiveness [3–6]. It is well accepted that the extra specific capacity of LRs originates from the participation of oxygen anion redox reaction at high voltage [7]. However, an irreversible oxygen release process ($2O^{2-} \rightarrow O_2$) inevitably occurs on the LR surface [8], resulting in the complex structural evolution and serious electrode/electrolyte side reaction [9, 10]. For example, the continual lattice oxygen loss accompanied by the formation of plentiful oxygen vacancies leads to irreversible migration of transition metal (TM) ions, and consequently gives rise to the phase transformation on the surface [6]. These structural degradations inevitably induce the erosion of the battery performance, including low initial Coulombic efficiency (ICE), capacity decay, voltage fade, and poor rate capability, which currently limit the commercial application of LRs [11].

To access scale application of LRs materials, stabilizing the structure of LRs and further optimizing the electrochemical performance is crucial. Due to the crippling degradation usually starts from the cathode surface and then impedes the efficient electrode reaction, it is necessary to build the secure surface to hold the structural stability. Common surface modification methods such as element doping [12], surface pretreatment [13], surface coating (AlF_3 [14], Li_3PO_4 [15], MgO [16], and Al_2O_3 [17]) have been widely used to optimize the electrochemical performance of cathode materials. *Ex-situ* coating strategies can achieve abundance options with flexible regulations, and thus coating surface modification becomes the promising method to alleviate the physical and chemical degradation of electrode material. However, some coating layer can only render one of the advantages in either electronic or ionic conductivity. Therefore, selecting the suitable materials as coating layer, which can manipulate both electronic and ionic conductivity of the cathodes, is still a great challenge.

In recent years, perovskite-like materials with K_2NiF_4-type structure have received considerable attention due to their good structural stability, excellent electrical conductivity, and ion diffusion kinetics [18–20]. For example, Heo et al. [19] prepared a composite cathode of $Li(Ni_{0.8}Co_{0.1}Mn_{0.1})O_2$ coated with garnet-

Address correspondence to wangxiaoguang@tyut.edu.cn, wangxiaog1982@163.com

type electrolyte and $La_2(Ni_{0.5}Li_{0.5})O_4$ nanoparticles. The excellent electrochemical performance of this modified cathode can be attributed to that the coated $La_2(Ni_{0.5}Li_{0.5})O_4$ nanoparticles exist high electrical conductivity and then facilitate the transport of lithium ions. Wu et al. [18] reported a modified cathode of $Li(Ni_{0.8}Co_{0.1}Mn_{0.1})O_2$ coated by $La_2Ni_{0.5}Li_{0.5}O_4$, which displayed significantly enhanced structural stability at high operating voltage and even long-cycling test. Density functional theory (DFT) calculations proved that $La_2Ni_{0.5}Li_{0.5}O_4$ and $LiNi_{0.8}Co_{0.1}Mn_{0.1}O_2$ possessed good structural compatibility, which is beneficial to the fast transport of Li ions. Yang et al. [20] found that the nickel-rich ternary cathode coated by $La_2Li_{0.5}Al_{0.5}O_4$ exhibited excellent cycling stability and rate performance. The main reason is that the $La_2Li_{0.5}Al_{0.5}O_4$ coating layer can not only expedite Li^+ transport but also prevent the erosion of the cathode material by the electrolyte. These works set the motivation to explore the potential of La-based perovskite-like material as coating layer for cathode substrate.

As a typical perovskite-like material, $La_2Li_{0.5}Co_{0.5}O_4$ (LLCO) is believed to be a promising coating layer to optimize the electrochemical properties of the cathodes because of its excellent electronic and ionic conductivity [21–23]. In this work, we select the LLCO as a suitable coating layer to homogeneously encapsulate the $Li_{1.2}Mn_{0.54}Ni_{0.13}Co_{0.13}O_2$ (LR) to tackle the above-mentioned issues for the first time. The unique composite (LR@LLCO) with homogeneously core–shell structure was synthesized by a solvothermal method combined with a wet chemical method. Experimental studies confirmed the crucial role of the uniform LLCO coating layer on the enhanced electrochemical performance. The LLCO surface not only provides the first shield to prevent the side reactions at the electrode/electrolyte interface, but also facilitates the reaction kinetic of composite electrode, which is ascribed to the high structural stability, excellent electrical conductivity, and fast Li-ion diffusion rate of perovskite-like LLCO. More importantly, the lanthanum owns the higher binding energy with oxygen (La–O = 799 kJ·mol^{-1}) compared with the previously reported elements (i.e., Al–O = 512 kJ·mol^{-1} and Mg–O = 394 kJ·mol^{-1}) [24, 25]. The high oxygen-affinity of La element makes LLCO capable of maintaining the lattice oxygen on the surface of LR, thereby improving its structural stability. This research demonstrates the ideal prospect of LLCO as decorated surface for high performance composite cathode materials of LIBs.

2 Experimental

2.1 Material preparation

Synthesis of LR sample: In a typical process, $LiCH_3COO{\cdot}2H_2O$ (5 wt.% excess), $Mn(CH_3COO)_2{\cdot}4H_2O$, $Ni(CH_3COO)_2{\cdot}4H_2O$, and $Co(CH_3COO)_2{\cdot}4H_2O$ were dissolved (with a molar ratio of 1.2:0.54:0.13:0.13) in ethanol and stirred to form a homogeneous solution. Meanwhile, oxalic acid (the molar ratio of oxalic acid to metal ions is 2.5:1) was also dissolved in ethanol to obtain an oxalic acid solution. During the uninterrupted stirring process, the oxalic acid solution was slowly added dropwise to the metal-ions solution and sustained reaction for 1 h. The resultant solution was transferred to a 100 mL Teflon-lined autoclave and then kept at 180 °C for 18 h. Afterward, the oxalate precursor was washed and collected by centrifuging several times, and dried. The LR was then synthesized by a heat-treatment at 450 °C for 5 h and then calcined at 900 °C. All chemicals were used as received without further purification in the experiment.

Synthesis of LR@LLCO samples: First, $La(NO_3)_3{\cdot}6H_2O$, $Co(CH_3COO)_2{\cdot}4H_2O$, and $LiNO_3$ were dissolved in ethanol with a molar ratio of 4:1:1. Then, the as-prepared LR powder was added into the above solution under stirring for 1 h. Next, the obtained solution was evaporated at 80 °C in continuous stirring process followed by sintering at 700 °C for 5 h. Afterward, the target LR@LLCO composite was obtained. Different composite samples were obtained by changing the predetermined feeding ratio of LLCO to LR. For simplicity, the samples that LR coated by 0.5 mol%, 1 mol%, 2 mol%, and 10 mol% LLCO, were named as 0.5LLCO, 1LLCO, 2LLCO, and 10LLCO, respectively. In addition, 0LLCO was prepared through the same procedure of 1LLCO without using reactants of LLCO.

2.2 Microstructure characterization

An X-ray diffractometer (XRD, DX2700) equipped with a copper Kα radiation source (40 kV, 30 mA, λ = 1.5406 Å) was used to examine the phases and crystallographic structure. The field emission scanning electron microscope (FESEM, JSM-7001F) and transmission electron microscope (TEM, JEM-2100F) with energy-dispersive X-ray spectrometer (EDX) were used to characterize the microstructure and element distribution of the prepared samples. The element valence state and chemical environment on the surface of the material were investigated by X-ray photoelectron spectroscopy (XPS, ESCALAB250XI) equipped with Al Kα radiation source (1486.68 eV).

2.3 Electrochemical measurements

The working electrodes were obtained by dispersing the active material, polyvinylidene fluoride (PVDF) (binder), and super-P (conductive agent) (with a weight ratio of 8:1:1) in N-methyl-2-pyridoxane (NMP), followed by stirring to form a homogeneous slurry. Subsequently, the slurry was evenly coated on the aluminum foil and vacuum-dried at 110 °C for 12 h. The diameter of the cathode electrodes was 14 mm and the mass loading of active material was about 2 mg·cm^{-2}. The CR2032 half-cell was assembled in an argon glove box, with lithium metal as the counter electrode and polypropylene membrane (Celgard 2400) as separators. The electrolyte was composed of 1 M lithium hexafluorophosphate ($LiPF_6$) dissolved in a mixed solution of ethylene carbonate (EC), dimethyl carbonate (DMC), and diethyl carbonate (DEC) with the volume ratio of 1:1:1. The rate and cycling performance of cell were measured through the LAND CT2001A testing system in a voltage range from 2.0 to 4.8 V (vs. Li/Li$^+$). For galvanostatic intermittent titration technique (GITT), the activated battery was firstly charged at a current density of 0.1 C for 10 min and then left to stand for 1 h in the voltage range from 2 to 4.8 V. Cyclic voltammetry (CV) was performed by Chenhua CHI760E electrochemical workstation. Electrochemical impedance spectroscopy (EIS) with a frequency range of 100 kHz to 0.01 Hz with a voltage amplitude of 5 mV was detected on the Chenhua CHI760E electrochemical workstation. The full-cell was constructed by using the commercial graphite as the anode material and the as-prepared sample as the cathode material. The preparation process of the anode was the same as that of the above cathode. The graphite electrode was firstly activated in a half-cell at 20 mA·g^{-1} for 5 cycles and then assembled with the prepared cathode to form a full-battery. The cut-off voltage range of full battery test was from 2 to 4.7 V.

3 Results and discussion

The LR@LLCO composites were synthesized through the conventional solvothermal method followed by a facile wet chemical method, as the schematic illustration shown in Fig. 1. The crystallite nature of prepared pristine LR and LR@LLCO with different scheduled coating amounts of 0.5 mol%, 1 mol%,

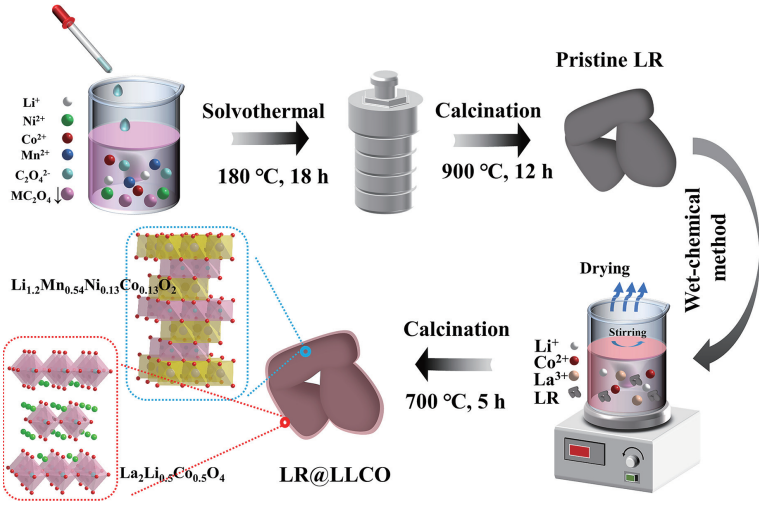

Figure 1 Schematic illustration for the preparation of LR@LLCO.

2 mol%, and 10 mol% LLCO (named as 0.5 LLCO, 1LLCO, 2LLCO, 10LLCO respectively) were measured by using XRD spectroscopy (Fig. S1 in the Electronic Supplementary Material (ESM)). According to the XRD patterns shown in Fig. S1(a) in the ESM, the pristine LR material and all LR@LLCO composites both exhibit the same main diffraction peaks. As observed, the typical reflections can be indexed with a hexagonal α-$NaFeO_2$ type layered phase (*R*3*m* space group) while the weak superlattice diffraction peaks around 22° ascribe to a monoclinic Li_2MnO_3 phase (*C*2/*m* space group) [8]. In addition, the characteristic reflections of LLCO can be obviously detected in the XRD pattern of 10LLCO (Fig. S1(b) in the ESM), indicating the successful construction of the LLCO coating layer. However, no peaks of LLCO can be observed in the XRD pattern of the other LR@LLCO composites, which should derive from the trace amount of the LLCO in these materials. In order to further analyze the changes in the crystalline structure after modification, the XRD rietveld refinement patterns of the LR and 1LLCO are shown in Figs. 2(a) and 2(b). Meanwhile, the corresponding crystalline structure parameters are summarized in Table S1 in the ESM. The lattice parameters *a* and *c* of the hexagonal layered phase are slightly increased after the LLCO modification, which may be caused by the doping of large radius of La^{3+} (0.1061 nm) or the formation of lithium vacancies [20, 26]. The increased lattice parameter *c* of the hexagonal layered phase is beneficial to reducing the ion diffusion barrier and then facilitates its rapid transmission in the bulk [27]. Meantime, the *c*/*a* ratio of the LR (~ 4.990) and 1LLCO (~ 4.991) is greater than that of the ideal cubic close-packed oxygen structure (~ 4.89), indicating that the as-obtained materials possess a good layered structure [28]. Moreover, 1LLLO has a smaller degree of cation mixing compared to the pristine LR. A small degree of Li/Ni mixing is conducive to maintaining the structural stability of the material, and thus leads to a better electrochemical performance for 1LLCO [29].

The surface morphology and coating microstructure of the LR@LLCO particles were investigated by using the scanning electron microscopy (SEM) and high-resolution transmission electron microscopy (HRTEM) characterizations. Figure 2(c) displays the SEM image of pristine LR particles. It is found these particles exhibit irregular morphology with a size of 200–600 nm. Such a microstructure is well maintained in the 1LLCO after the coating process, as shown in Fig. 2(d), demonstrating that the LLCO modification would not affect the morphology of the LR substrate. Further, as shown in Fig. 2(e), the HRTEM image of the 1LLCO exhibits a distinct interface between the core and shell (highlighted by a dash line), indicating that the LLCO coating was successfully decorated on the LR surface. Moreover, the enlarged view of selected area in Fig. 2(e) is shown in Fig. 2(f). As observed, the LLCO coating layer possesses a homogeneous thickness of ca. 16 nm. In addition, the measured *d*-spacing of the surface phase is ca. 0.14 nm, being indexed to the (215) plane of LLCO. The interplanar spacing of ca. 0.47 nm of the core phase corresponds to the (003) plane of $LiMO_2$ (M = Ni, Co, and Mn) with typical layered structure [30], which is in good agreement with the results of XRD. To further confirm the uniformity of the coating, the energy-dispersive X-ray spectroscopy (EDX) elemental mapping was conducted on the 1LLCO particles. Figure 2(g) and Fig. S2 in the ESM reveal the homogeneous distribution of Ni, Co, Mn, O, and La elements at the particles, further verifying the coating structure of the 1LLCO. It should be pointed out that there were differences for the thickness of LLCO coating layer in different regions, as exhibited in Fig. S2 in the ESM, and the thickness of coating layer was from 5 to 16 nm. The difference may be attributed to the experimental error during wet chemical method, and the lattices-mismatched features between the LLCO-precursor, crystalline LLCO and LR.

XPS was further used to analyze the chemical valence state and surface bonding configuration of the as-obtained samples (pristine LR and 1LLCO). As shown in Fig. 3(a), the Ni 2p peaks of the pristine LR and 1LLCO display no obvious shift and the Ni $2p_{3/2}$ peak at 854.3 eV corresponds to Ni^{2+} [31]. It is worth noting that, compared with the pristine LR, there is an additional peak at 851.1 eV in the Ni 2p XPS spectra of 1LLCO sample (Fig. 3(a)), which can be assigned to the La $3d_{3/2}$ peak. The inevitable peak overlap of Ni 2p and La 3d is ascribed to the relatively closed binding energies, and this phenomenon has also been observed in the previous reports [32, 33]. As shown in Fig. 3(b), the peak at 854.3 eV corresponds to the Ni $2p_{3/2}$. From the La 3d XPS spectra, it is found that the 1LLCO has a typical La 3d characteristic peak, and the peak at 834.3 eV corresponds to the La^{3+} [34], which is consistent with the valence state of La in LLCO. On the contrary, no La 3d peak can be found in the pristine LR, indicating the successful decoration of the LLCO coating in the composite. The O 1s XPS spectra of the pristine LR and 1LLCO are displayed in Fig. 3(c), in which the O 1s peak can be fitted into lattice oxygen, oxygen vacancy, and CO_3^{2-} with the binding energy of 529.2, 531.0, and 532.4 eV, respectively [35]. It can be found that the content of oxygen vacancies has increased by 16.4% after LLCO modification, demonstrating the oxygen-deficient feature of the LLCO coating layer [36, 37]. The existence of oxygen vacancies can reduce irreversible oxygen release, increase electronic conductivity, and enhance Li^+ diffusion rate [37, 38], resulting in

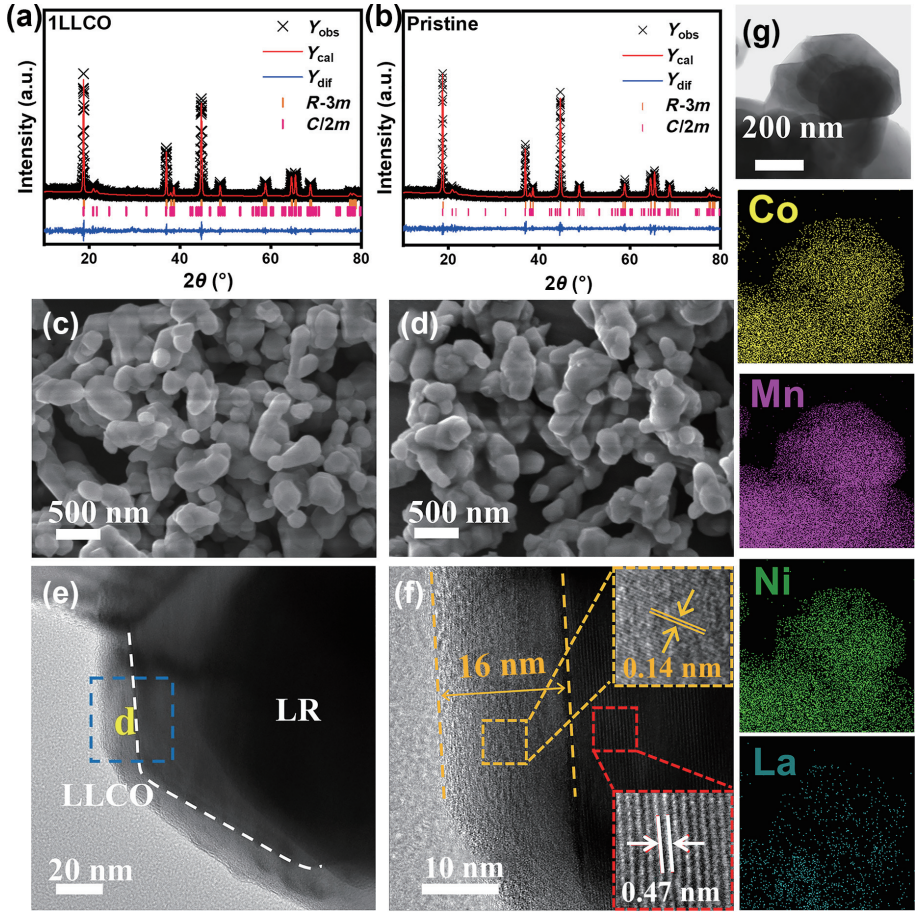

Figure 2 XRD Rietveld refinement profiles of (a) LR and (b) 1LLCO. SEM images of (c) LR and (d) 1LLCO samples. (e) HRTEM image of 1LLCO particle. (f) Selected region enlarged view of (e). (g) EDX mappings of 1LLCO.

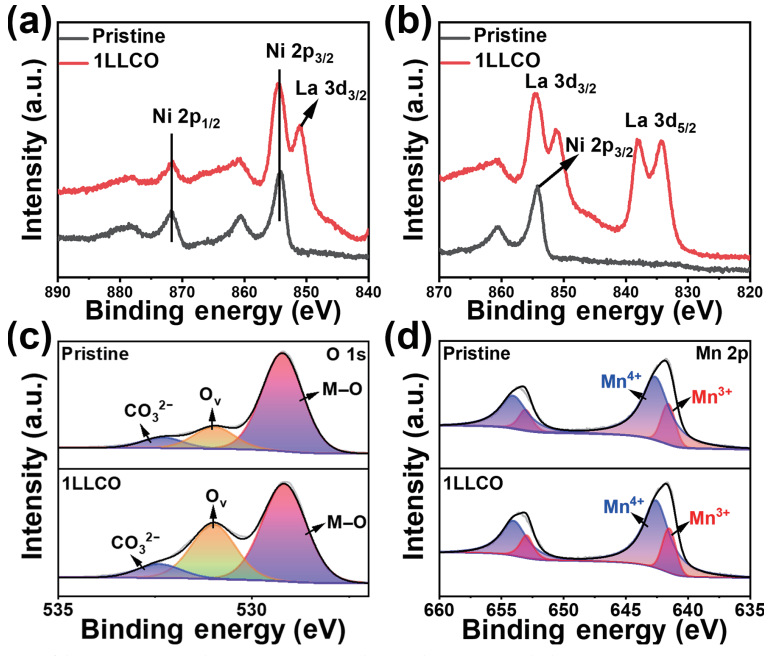

Figure 3 High-resolution XPS spectra of the pristine LR and 1LLCO. (a) Ni 2p, (b) La 3d, (c) O 1s, and (d) Mn 2p.

an excellent structural stability and reaction kinetic. In Fig. 3(d), Mn^{3+} (641.5 eV) and Mn^{4+} (642.6 eV) coexist in both two samples [27]. The content of Mn^{3+} in the 1LLCO is increased by 6.3% compared with that of pristine LR, which is related to compensate for the non-conservation of charge caused by oxygen vacancies. The Co 2p XPS spectra of the pristine LR and 1LLCO samples are presented in Fig. S3 in the ESM. The binding energy of 779.5 and 780.4 eV is attributed to Co^{3+} and Co^{2+} [36], and the ratio of Co^{2+}/Co^{3+} is increased after the introduction of the LLCO layer, indicating the lower valence state of cobalt and abundant oxygen vacancies in the LLCO coating layer, which may ascribe to the high oxygen-affinity of La element.

Electrochemical performance and physicochemical superiority of the modified LR@LLCO mentioned above were evaluated in coin-type half cells, using the fabricated samples as electrode material and Li piece as counter electrode, respectively. Figures

4(a)–4(c) display the CV curves of the initial three cycles of the LR and 1LLCO cathodes, respectively. In the first cycle, both LR and 1LLCO have two oxidation peaks at about 4.0 and 4.6 V in the first charge process. The oxidation peaks at 4.0 V correspond to the oxidation of Ni^{2+} and Co^{3+} in $LiMO_2$ to higher valence states (Ni^{3+}, Ni^{4+}, and Co^{4+}), along with the deintercalation of Li^+ [39]. In the second and third cycles, compared with the pristine LR, 1LLCO shows a higher current density at 4.0 V and the corresponding peak position is slightly shifted to the lower voltage direction, indicating that Ni/Co ions are more stably involved in the oxidation process in the 1LLCO [29]. Without the protection of the LLCO coating layer, the Ni/Co ions in pristine LR tend to react with the electrolyte, which eventually results in the loss of TM ions and high irreversibility. It should be emphasized that the 1LLCO exhibits a lower oxidation peak at 4.6 V than that of LR in the initial charge reaction, indicating that the irreversible part of Li_2MnO_3 activation is inhibited by the LLCO modification [40]. The inhibitory effect is caused by the high oxygen affinity of La element, which can stabilize the lattice oxygen on the LR surface, and then reduce the irreversible release of oxygen during the initial charge process [33, 41]. However, the higher current densities of the 1LLCO at 4.6 V in the following cycles demonstrate the high reversible degree of Li_2MnO_3 activation participating in the charge process [40], further revealing the enhanced structural stability of the 1LLCO. For the discharge process, the reduction peaks at about 4.5 and 3.7 V correspond to the reduction of high-valence Ni/Co ions, and the reduction peak at about 3.4 V relates to the $Mn^{4+} \rightarrow Mn^{3+}$ [27, 42]. The latter peak of the 1LLCO exhibits lower current intensity than those of LR, indicating that the irreversible loss of Li_2O is decreased and the reversibility of oxygen redox reaction is increased in the activation process of Li_2MnO_3 [27]. These results verify the important role of the LLCO coating layer on the suppression of irreversible lattice oxygen release, TM-ions migration, and phase transformation in the surface of LR substrate. Figure 4(d) shows the initial charge and discharge curves of all samples at 0.1 C (1 C = 250 $mA{\cdot}g^{-1}$) in the voltage range of 2–4.8 V. The specific discharge capacities of the pristine LR, 0.5LLCO, 1LLCO, and 2LLCO are 266.2, 270.5, 269.1, and 247.4 $mAh{\cdot}g^{-1}$, respectively. The 1LLCO cathode shows a large ICE of 81.2%, higher than those of the LR (77.5%), 0.5LLCO (79.3%), and 2LLCO (79.8%), respectively. As shown in Fig. 4(e), the 1LLCO has the best rate performance among all samples, and its discharge capacities at 0.1, 0.2, 0.5, 1, 2, and 5 C are 269.1, 258.2, 231.4, 205.7, 177.6, and 136.7 $mAh{\cdot}g^{-1}$, respectively. Additionally, the capacity reversibility of 1LLCO is as high as 100.5% (270.5 $mAh{\cdot}g^{-1}$) when the current density returned to 0.1 C. The higher specific capacity of the 1LLCO after rate test may be attributed to the slow activation process of coating-modified cathode materials. The superior capacity reversibility and rate performance are mainly ascribed to high Li^+/electronic conductivity of the LLCO coating layer and the improved structural stability of cathode.

Cyclic lifespan of the prepared samples at different current densities was recorded to further investigate the influence of the LLCO modification. As shown in Fig. S4(a) in the ESM, 1LLCO exhibits a great capacity retention of 95.2% after 100 cycles at 0.1 C, while the untreated LR only shows a capacity retention of 79.5% after same cycles. When cycled at 1 C, the discharge

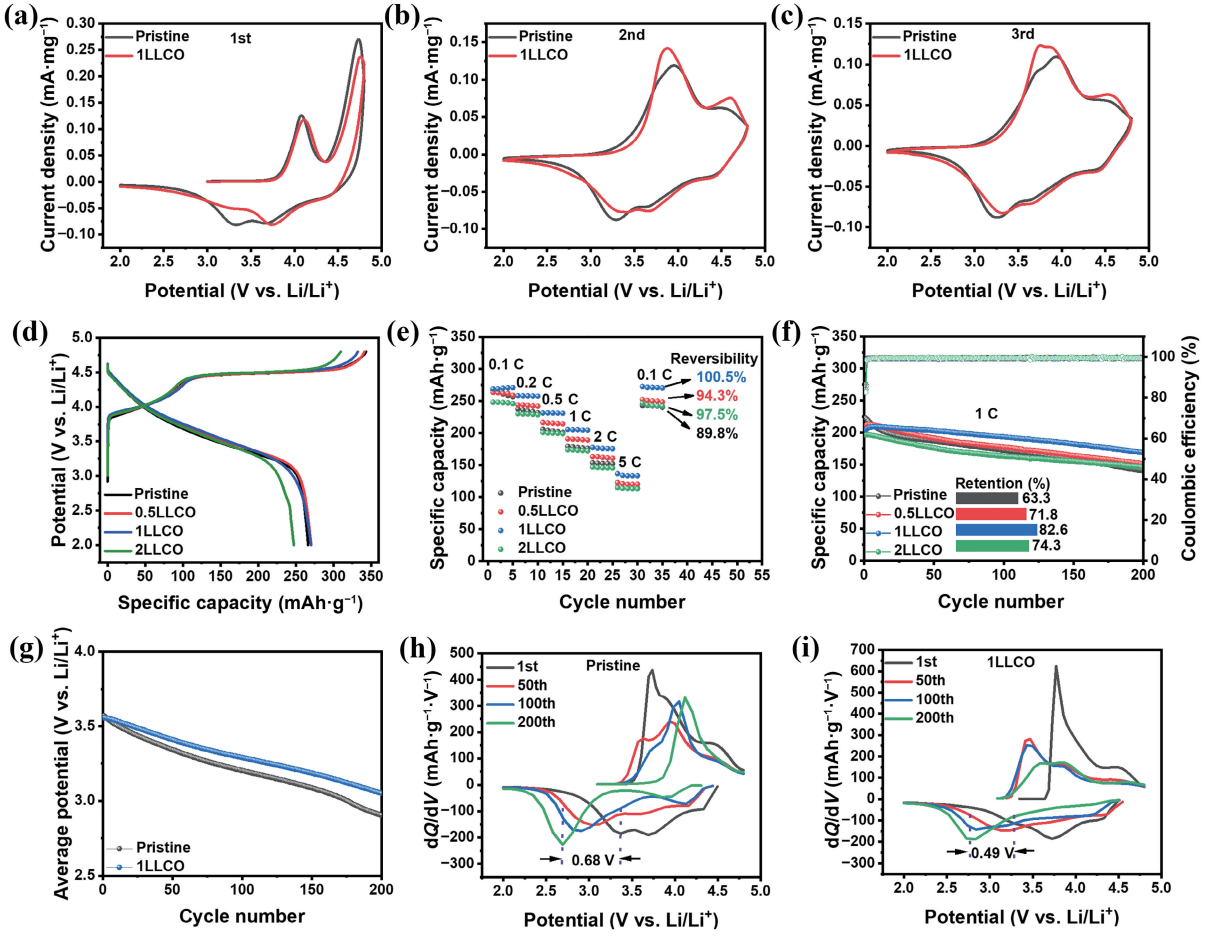

Figure 4 CV curve of the (a) first, (b) second and (c) third cycle for the pristine LR and 1LLCO cathodes at a scan rate of 0.1 $mV{\cdot}s^{-1}$. (d) The initial charge–discharge curves of all cathodes at 0.1 C. (e) Rate performance of the LR and LR@LLCO cathodes. (f) Cycling performance of the LR and LR@LLCO cathodes at 1 C. (g) Average discharging voltage vs. cycle number of the LR and 1LLCO cathodes. The dQ/dV curves of different cycles for the pristine (h) LR and (i) 1LLCO at 1 C.

capacity of the 1LLCO is maintained at 168.7 mAh·g^{-1} with retention of 82.6% after 200 cycles (Fig. 3(f)). However, the discharge capacities of the pristine LR, 0.5LLCO, and 2LLCO decline to 141, 151.5, and 146 mAh·g^{-1} after 200 cycles, with the capacity retentions of 63.3%, 71.8%, and 74.3%, respectively. When cycled at a higher current density of 2 C, as depicted in Fig. S4(b) in the ESM, 1LLCO still delivers a higher capacity retention of 78.7% than that of pristine LR (64.4%). Figure S5 in the ESM exhibits the cycling capacities of the 0LLCO and LR, and the similar downward trend reveals that only the wet chemical process without LLCO could not improve the structural stability of LR matrix. Moreover, as exhibited in Fig. 4(g), the average discharge voltage attenuation of the 1LLCO is superior to that of pristine LR after 200 cycles, demonstrating that the introduction of LLCO can also suppress the voltage decay of LR and then result in high energy retentions. In order to investigate the trend of voltage decay in detail, dQ/dV plots are depicted in Figs. 4(h) and 4(i). The reduction peak at 3.4 V corresponds to the reduction of Mn^{4+}. This peak shifts to a low voltage during the cycling process, which is related to the formation of the spinel phase [15]. The pristine LR shifted by 0.68 V after 200 cycles at 1 C while the 1LLCO shifted by only 0.49 V. These results indicate that the LLCO coating can suppress the phase transition from the layer phase to the spinel phase and alleviate the voltage degradation of the LR cathode [15, 35]. The effective influence on improving the structural stability can be attributed to the strong La–O bond, which is beneficial to suppressing the irreversible loss of surface lattice oxygen of LRs cathodes during cycling, and thereby alleviating the occurrence of surface reconstruction and phase transition.

To understand the enhancement mechanism on electrochemical performance, CV measurement was carried out for the pristine LR and 1LLCO at various scan rates, as shown in Figs. 5(a) and 5(b). With increasing of scan rates, the locations of both oxidation and reduction peaks of 1LLCO show a more neglectful shift to the sides than that of LR cathode, revealing the small polarization of 1LLCO caused by the enhanced reaction kinetic. Based on the CV curves, two oxidation and reduction peaks (marked as O1 and R1) were selected to qualitatively analyze the Li^+ diffusion coefficient (D_{Li^+}) according to the Randles–Sevcik equation, and the fitted straight line of O1 and R1 is displayed in Figs. 5(c) and 5(d), respectively.

It can be found that the 1LLCO cathode owns a larger slope during charging and discharging, evidencing that the 1LLCO possesses the faster Li^+ diffusion kinetics. In addition, the GITT was further utilized to investigate the Li^+ diffusion kinetic of the 1LLCO cathode. Figures 5(e) and 5(f) display the D_{Li^+} values of the LR and 1LLCO cathodes during charge and discharge process, respectively, and the corresponding values for 1LLCO are both higher than that of LR cathode. When charged to 4 V, the D_{Li^+} of the 1LLCO is 8.30×10^{-11} cm^2·s^{-1}, while the D_{Li^+} of the original LR is only 4.37×10^{-11} cm^2·s^{-1}. Moreover, when re-discharged to 4 V again, the value of D_{Li^+} for the 1LLCO still reaches to 1.24×10^{-10} cm^2·s^{-1}, higher than 7.82×10^{-11} cm^2·s^{-1} for LR. The results manifest that the modified 1LLCO exhibits the great Li^+ transport capacity during electrochemical reaction process due to the high ionic conductivity of the LLCO coating layer on the surface of pristine LR materials.

The charge transfer ability and interfacial reaction resistance of the prepared cathodes were evaluated by EIS measurement. As shown in Fig. S6 in the ESM, the Nyquist plots of all samples consist of a semicircle and a straight line. The semicircle at high frequency represents the charge transfer resistance (R_{ct}) at interface and the straight line at high frequency is related to Warburg impedance (W_s) for ions diffusion. After coated by the LLCO layer, the R_{ct} values of cathodes are both decreased, implying the introduction of LLCO can greatly lower the interface

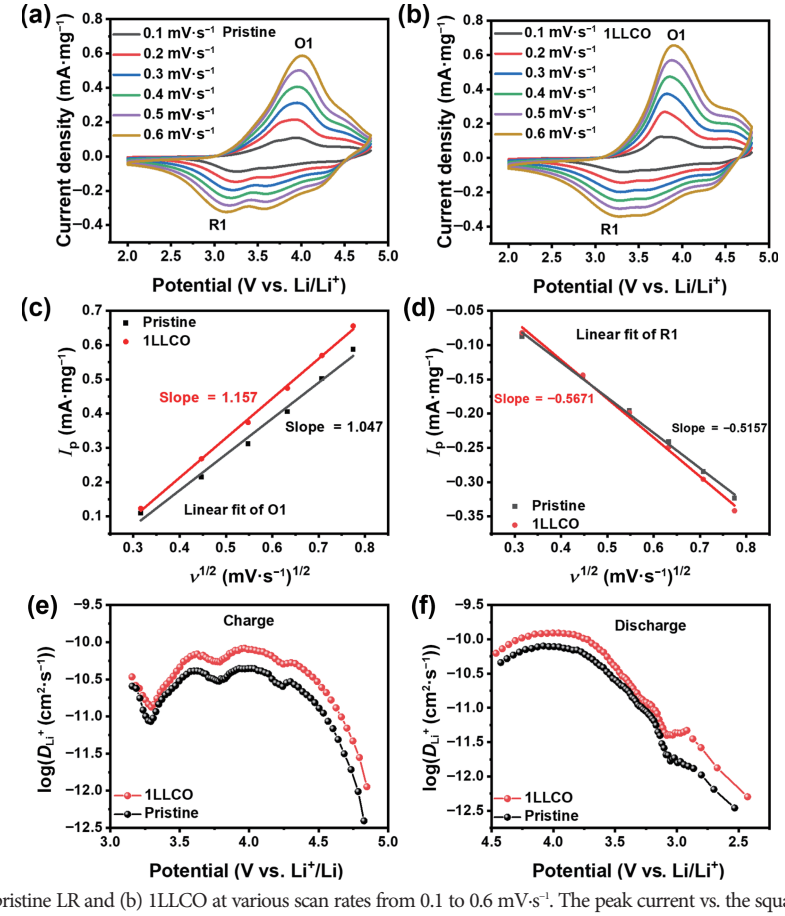

Figure 5 CV curves of the (a) pristine LR and (b) 1LLCO at various scan rates from 0.1 to 0.6 mV·s^{-1}. The peak current vs. the square root of scanning rate ($v^{1/2}$) plots of the two samples: the linear fit of (c) O1 and (d) R1. Li^+ diffusion coefficients of (e) pristine LR and (f) 1LLCO during charge and discharge process.

resistance and facilitate the ions/electrons transport on the interface between electrode and electrolyte, which is attributed to the optimized thickness of cathode electrolyte interfaces (CEIs) and high electrical conductivity of perovskite-type LLCO. It is worth noting that the 1LLCO exhibits the lowest R_{ct} value among all modified cathodes, indicating the vital role of moderate coating on charge/discharge reactions, which results in the optimal electrochemical performance.

In order to further explore the effect of the LLCO modification on LR, the microstructure of the pristine LR and 1LLCO cathodes after cycling were characterized in detail. Figures 6(a) and 6(b) show the SEM images of the pristine LR and 1LLCO after 200 cycles at 1 C, respectively. It can be found that some microcracks around 100 nm appear on the surface of the pristine LR particles after cycling owing to the anisotropic volume changes, phase transition, and electrolyte corrosion. The widespread existence of evolved microcracks on the LR surface inevitably leads to the capacity fade and voltage decay during the cycling. In contrast, the structure of the 1LLCO secondary particles is well maintained as shown in Fig. 6(b) on account of the protection of the LLCO coating layer. It is obvious the LLCO shell can act as a physical barrier to effectively protect the bulk LR phase from corrosion, and mitigate the inner anisotropic strain during cycling process. Furthermore, the crystal phases of the corresponding electrodes after cycling were also evaluated by XRD. As depicted in Fig. 6(c) and Fig. S7 in the ESM, XRD results reveal that two samples both show well-preserved layered structure after cycling. It can be found that the (003) and (104) diffraction peaks of the pristine LR electrode are slightly shifted to high angles compared with that of 1LLCO electrode after cycling, while the peak locations of the 1LLCO keep in initial position, which is resulted from the severe structure collapse of LR substrate without the LLCO decoration due to the continuous TM migration and phase transition, as well as the irreversible oxygen release during long-term cycling [11]. Moreover, surface conditions of the pristine LR and 1LLCO cathodes after cycling were investigated through XPS. As shown in Fig. 6(d), the Mn 2p spectra can be fitted to Mn^{3+} and Mn^{4+} with binding energies of 641.3 and 642.9 eV, respectively [42]. It has been widely accepted that Mn^{3+} triggers severe Jahn–Teller distortion and disproportionation reactions, resulting in degradation of the structure and electrochemical performance [43]. After 200 cycles, the content of Mn^{3+} in the 1LLCO was reduced by 24.4% compared with the pristine sample, which is conducive to suppressing the Jahn–Teller effect, restraining the phase transformation from the layer phase to the spinel phase ($LiMn_2O_4$), and then improved cycling stability of the LR substrate. In Fig. 6(d), the F 1s spectra both consist of two peaks, which are assigned to LiF (684.93 eV) and C–F (687.48 eV) [44].

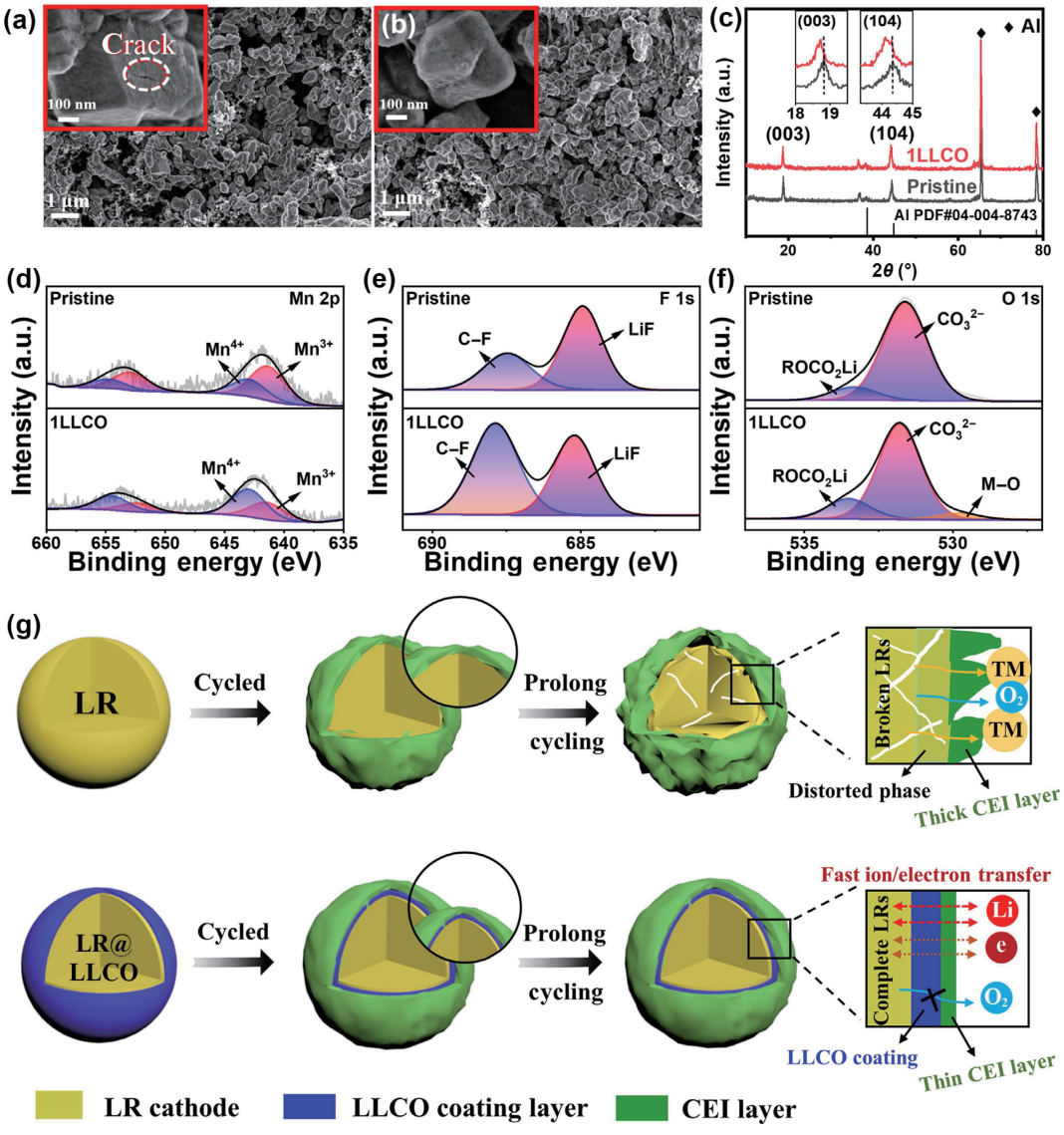

Figure 6 SEM images of the (a) pristine LR and (b) 1LLCO cathodes after 200 cycles at 1 C. (c) XRD patterns of the above samples. High-resolution XPS spectra of (d) Mn 2p, (e) F 1s, and (f) O 1s. (g) Schematic diagram of microstructure evolution during the electrochemical cycling process of the pristine LR and 1LLCO cathodes.

As the important indicator for CEI, LiF, derived from the decomposition of $LiPF_6$, will greatly influence the interface impedance for ion and electron transport. The reduced peak area of LiF in the 1LLCO indicates that the undesirable side reaction between the cathode material and the electrolyte is suppressed due to the construction of the LLCO coating on the surface, resulting in the improvement of electrochemical interface stability. In addition, the O 1s XPS spectrum of the 1LLCO consists of three oxygen species located at 529.78, 531.8, and 533.51 eV, which are assigned to lattice oxygen, CO_3^{2-}, and electrolyte oxidation species ($ROCO_2Li$), respectively [29, 32]. However, no lattice oxygen was detected in the pristine samples because of the formation of thick passivation layer and the dissolution of plenty of TM on LR surface.

Based on the above results, the efficient multiple effects of the LLCO modification on LR substrate are schematically illustrated in Fig. 6(g). The LLCO decorating layer can effectively stabilize the lattice oxygen release, inhibit the TM migration and phase distortion. Thus, the integrity maintenance of surrounded LR particle not only facilitates ion diffusion and electron transfer but also suppresses the side reaction between LR and electrolyte, and reduces the thickness of the passivation layer on the cathode surface. Therefore, the LR@LLCO cathode possesses excellent electrochemical performances including great rate performance, excellent cycling stability, and decreased voltage decay, which is better or competitive compared with the previous reports (as shown in Table S2 in the ESM).

The optimized electrochemical performance of 1LLCO motivates us to further evaluate its potential in practical application. Herein, commercial graphite was used as the anode, coupled by the pristine LR or 1LLCO as the cathode to assemble the full-cell, as illustrated in Fig. 7(a). The suitable voltage range of 2–4.7 V was applied to evaluate the electrochemical performance for the LR//graphite and 1LLCO//graphite full-cells. Figure 7(b) displays the initial charge–discharge curves of two full-cells at 0.1 C. It is found that the 1LLCO//graphite affords a higher ICE (73.3%) compared with that of the LR//graphite (71.3%). Furthermore, the 1LLCO//graphite full-cell exhibits the excellent discharge capacities of 250.7 and 117.2 mAh·g^{-1} at 0.1 and 5 C (Fig. 7(c)), respectively. When the current density returns to 0.1 C, the 1LLCO//graphite full-cell still delivers a discharge capacity of 187.3 mAh·g^{-1}, which is higher than that of the LR//graphite full battery (163.2 mAh·g^{-1}), demonstrating the enhanced structural stability and reversibility of 1LLCO cathode. Cycling performance of two kinds of full-cell was also measured and depicted in Fig. 7(d). The discharge capacity of 1LLCO//graphite full-cell is still maintained as high as 70.0% even after 200 cycles test at 1 C, while it is 54.8% for LR//graphite, further verifying the structural stability of 1LLCO. In addition, a green LED pattern can be successfully lighted up by one 1LLCO//graphite full-cell (inset of Fig. 7(d)), displaying the promising prospect of 1LLCO in practical application.

4 Conclusion

In this work, perovskite-like LLCO was successfully constructed on the surface of the LR material as advance core@shell composite cathode for LIBs. The LLCO coating layer with high oxyphilicity of La element can act as an inhibitor for the lattice oxygen release, TM atom migration, as well as phase transformation. Meanwhile, the decorated LLCO also plays a crucial role as a physical barrier to minimize the side reactions at electrode/electrolyte interface, suppress TM dissolution, and release internal stress during charge–discharge process. Additionally, the high electronic and ionic conductivity of the LLCO guarantee the fast charge transfer and unobstructed ions transport for cathode material with superior reaction kinetics. As a consequence, the modified 1LLCO composite exhibits a surprising capacity retention of 95.21% with high capacity of 250.6 mAh·g^{-1} after 100 cycles at 0.1 C and still possesses the specific capacity of 168.7 mAh·g^{-1} with 82.6% capacity retention after 200 cycles at 1 C. The excellent cycling stability and rate performance induced by the LLCO coating modification demonstrates that the present work provides a promising idea for the design of advanced layered cathode materials.

Acknowledgements

This work was supported by the National Natural Science Foundation of China (Nos. 21878201 and 22008165), the Natural Science Foundation of Shanxi Province (No. 20210302124211), the Scientific and Technological Innovation Programs of Higher Education Institutions in Shanxi (No. 2021L042), the Foundation of Taiyuan University of Technology (No. 2022QN022), and the 7th Youth Talent Support Program of Shanxi Province.

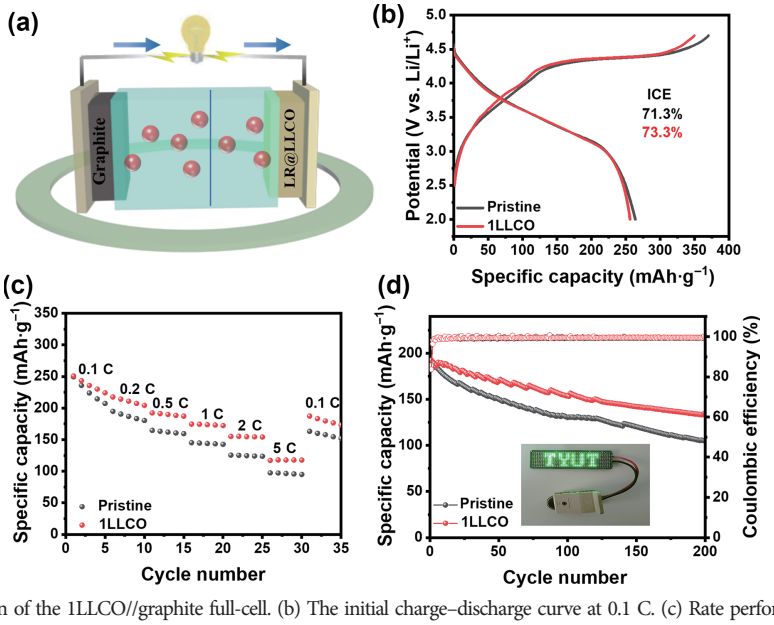

Figure 7 (a) Schematic illustration of the 1LLCO//graphite full-cell. (b) The initial charge–discharge curve at 0.1 C. (c) Rate performance. (d) Cycling performance obtained at 1 C of the LR//graphite and 1LLCO//graphite full-cell in the voltage range of 2–4.7 V.

Electronic Supplementary Material: Supplementary material (XRD patterns, elemental distribution and line scanning results, high-resolution Co 2p XPS spectra, cycling performance, electrochemical impedance spectra, refine crystal structure parameters, and comparison of the electrochemical performances) is available in the online version of this article at https://doi.org/10.1007/s12274-023-5613-2.

References

[1] He, W.; Guo, W. B.; Wu, H. L.; Lin, L.; Liu, Q.; Han, X.; Xie, Q. S.; Liu, P. F.; Zheng, H. F.; Wang, L. S. et al. Challenges and recent advances in high capacity Li-rich cathode materials for high energy density lithium-ion batteries. *Adv. Mater.* **2021**, *33*, 2005937.

[2] Chen, Y. F.; Liu, Y. C.; Zhang, J. C.; Zhu, H.; Ren, Y.; Wang, W.; Zhang, Q.; Zhang, Y.; Yuan, Q. H.; Chen, G. X. et al. Constructing O2/O3 homogeneous hybrid stabilizes Li-rich layered cathodes. *Energy Storage Mater.* **2022**, *51*, 756–763.

[3] Chen, B. Z.; Zhao, B. C.; Zhou, J. F.; Fang, Z. T.; Huang, Y. N.; Zhu, X. B.; Sun, Y. P. Surface modification with oxygen vacancy in Li-rich layered oxide Li1.2Mn0.54Ni0.13Co0.13O2 for lithium-ion batteries. *J. Mater. Sci. Technol.* **2019**, *35*, 994–1002.

[4] Liu, Y. C.; Chen, Y. F.; Wang, J.; Wang, W.; Ding, Z. Y.; Li, L. Y.; Zhang, Y.; Deng, Y. D.; Wu, J. W.; Chen, Y. N. Hierarchical yolk–shell structured Li-rich cathode boosting cycling and voltage stabled LIBs. *Nano Res.* **2022**, *15*, 3178–3186.

[5] Liu, Y. C.; Zhu, H.; Zhu, H. K.; Ren, Y.; Zhu, Y. Z.; Huang, Y. L.; Dai, L.; Dou, S. M.; Xu, J.; Sun, C. J. et al. Modulating the surface ligand orientation for stabilized anionic redox in Li-rich oxide cathodes. *Adv. Energy Mater.* **2021**, *11*, 2003479.

[6] Liu, T. C.; Liu, J. J.; Li, L. X.; Yu, L.; Diao, J. C.; Zhou, T.; Li, S. N.; Dai, A.; Zhao, W. G.; Xu, S. Y. et al. Origin of structural degradation in Li-rich layered oxide cathode. *Nature* **2022**, *606*, 305–312.

[7] Gou, X. X.; Hao, Z. K.; Hao, Z. M.; Yang, G. J.; Yang, Z.; Zhang, X. Y.; Yan, Z. H.; Zhao, Q.; Chen, J. In situ surface self-reconstruction strategies in Li-rich Mn-based layered cathodes for energy-dense Li-ion batteries. *Adv. Funct. Mater.* **2022**, *32*, 2112088.

[8] Zhang, C. X.; Feng, Y. Z.; Wei, B.; Liang, C. P.; Zhou, L. J.; Ivey, D. G.; Wang, P.; Wei, W. F. Heteroepitaxial oxygen-buffering interface enables a highly stable cobalt-free Li-rich layered oxide cathode. *Nano Energy* **2020**, *75*, 104995.

[9] Si, M. T.; Wang, D. D.; Zhao, R.; Pan, D.; Zhang, C.; Yu, C. Y.; Lu, X.; Zhao, H. L.; Bai, Y. Local electric-field-driven fast Li diffusion kinetics at the piezoelectric LiTaO3 modified Li-rich cathode–electrolyte interphase. *Adv. Sci.* **2020**, *7*, 1902538.

[10] Wang, E. R.; Zhao, Y.; Xiao, D. D.; Zhang, X.; Wu, T. H.; Wang, B. Y.; Zubair, M.; Li, Y. Q.; Sun, X. L.; Yu, H. J. Composite nanostructure construction on the grain surface of Li-rich layered oxides. *Adv. Mater.* **2020**, *32*, 1906070.

[11] He, W. T.; Zhang, C. X.; Wang, M. Y.; Wei, B.; Zhu, Y. L.; Wu, J. H.; Liang, C. P.; Chen, L. B.; Wang, P.; Wei, W. F. Countering voltage decay, redox sluggishness, and calendering incompatibility by near-zero-strain interphase in lithium-rich, manganese-based layered oxide electrodes. *Adv. Funct. Mater.* **2022**, *32*, 2200322.

[12] Boivin, E.; Guerrini, N.; House, R. A.; Lozano, J. G.; Jin, L. Y.; Rees, G. J.; Somerville, J. W.; Kuss, C.; Roberts, M. R.; Bruce, P. G. The role of Ni and Co in suppressing O-loss in Li-rich layered cathodes. *Adv. Funct. Mater.* **2021**, *31*, 2003660.

[13] Lin, T. E.; Schulli, T. U.; Hu, Y. X.; Zhu, X. B.; Gu, Q. F.; Luo, B.; Cowie, B.; Wang, L. Z. Faster activation and slower capacity/voltage fading: A bifunctional urea treatment on lithium-rich cathode materials. *Adv. Funct. Mater.* **2020**, *30*, 1909192.

[14] Zheng, J. M.; Gu, M.; Xiao, J.; Polzin, B. J.; Yan, P. F.; Chen, X. L.; Wang, C. M.; Zhang, J. G. Functioning mechanism of AlF3 coating on the Li- and Mn-rich cathode materials. *Chem. Mater.* **2014**, *26*, 6320–6327.

[15] Su, Y. F.; Yuan, F. Y.; Chen, L.; Lu, Y.; Dong, J. Y.; Fang, Y. Y.; Chen, S.; Wu, F. Enhanced high-temperature performance of Li-rich layered oxide via surface heterophase coating. *J. Energy Chem.* **2020**, *51*, 39–47.

[16] Shi, S. J.; Tu, J. P.; Tang, Y. Y.; Liu, X. Y.; Zhang, Y. Q.; Wang, X. L.; Gu, C. D. Enhanced cycling stability of Li[Li0.2Mn0.54Ni0.13Co0.13]O2 by surface modification of MgO with melting impregnation method. *Electrochim. Acta* **2013**, *88*, 671–679.

[17] Wen, X. F.; Liang, K.; Tian, L. Y.; Shi, K. Y.; Zheng, J. S. Al2O3 coating on Li1.256Ni0.198Co0.082Mn0.689O2.25 with spinel–structure interface layer for superior performance lithium ion batteries. *Electrochim. Acta* **2018**, *260*, 549–556.

[18] Wu, F.; Li, Q.; Chen, L.; Zhang, Q. Y.; Wang, Z. R.; Lu, Y.; Bao, L. Y.; Chen, S.; Su, Y. F. Improving the structure stability of LiNi0.8Co0.1Mn0.1O2 by surface perovskite-like La2Ni0.5Li0.5O4 self-assembling and subsurface La3+ doping. *ACS Appl. Mater. Interfaces* **2019**, *11*, 36751–36762.

[19] Heo, K.; Lee, J.; Im, J.; Kim, M. Y.; Kim, H. S.; Ahn, D.; Kim, J.; Lim, J. A composite cathode material encapsulated by amorphous garnet-type solid electrolyte and self-assembled La2(Ni0.5Li0.5)O4 nanoparticles for all-solid-state batteries. *J. Mater. Chem. A* **2020**, *8*, 22893–22906.

[20] Yang, J. C.; Chen, Y. X.; Li, Y. J.; Deng, S. Y.; Chang, S. H.; Cao, G. L.; Zhang, D. W.; Wang, S. L.; Li, W. A simple strategy to prepare the La2Li0.5Al0.5O4 modified high-performance Ni-rich cathode material. *Mater. Chem. Phys.* **2020**, *249*, 123135.

[21] Ghosh, P.; Mahanty, S.; Basu, R. N. Lanthanum-doped LiCoO2 cathode with high rate capability. *Electrochim. Acta* **2009**, *54*, 1654–1661.

[22] Yin, H. X.; Long, Y.; Liu, Y. J.; Cui, Y. C.; Hao, C. C.; Lei, Q. Q. Effect of La2Li0.5Co0.5O4 in semiconductive nanocomposites on suppression of space charge injection to the insulating medium for high-voltage direct current cables. *Mater. Lett.* **2021**, *296*, 129895.

[23] Shi, H. C.; Zeng, T. Y.; Zhang, H. W.; Zhou, Y.; Su, M. R.; Li, X. W.; Zhang, P. P.; Dou, A. C.; Naveed, A.; Liu, Y. J. Enhanced structure and electrochemical stability of single crystal nickel-rich cathode material by La2Li0.5Co0.5O4 surface coating. *Ceram. Int.* **2022**, *48*, 17548–17555.

[24] Xie, Y.; Hu, X. Y.; Shi, N.; Peng, R. R.; Chen, M.; Xia, C. R. La-doped Ba0.5Sr0.5Co0.8Fe0.2O3-d as cathode for protonic-conducting solid oxide fuel cells with enhanced structure stability. *ECS Trans.* **2021**, *103*, 1525–1535.

[25] Li, M.; Deng, X. Y.; Wang, Z. X.; Liu, K.; Ma, Z. Z.; Wang, J. X.; Wang, X. G. Heterostructured lithium-rich layered oxides core@spinel-MgAl2O4 shell as high-performance cathode for lithium-ion batteries. *Appl. Surf. Sci.* **2022**, *592*, 153328.

[26] Liu, P. F.; Zhang, H.; He, W.; Xiong, T. F.; Cheng, Y.; Xie, Q. S.; Ma, Y. T.; Zheng, H. F.; Wang, L. S.; Zhu, Z. Z. et al. Lithium deficiencies engineering in Li-rich layered oxide Li1.098Mn0.533Ni0.113Co0.138O2 for high-stability cathode. *J. Am. Chem. Soc.* **2019**, *141*, 10876–10882.

[27] Li, S. Y.; Fu, X. L.; Liang, Y. W.; Wang, S. X.; Zhou, X. A.; Dong, H.; Tuo, K. Y.; Gao, C. K.; Cui, X. L. Enhanced structural stability of boron-doped layered@spinel@carbon heterostructured lithium-rich manganese-based cathode materials. *ACS Sustainable Chem. Eng.* **2020**, *8*, 9311–9324.

[28] Wu, B.; Yang, X. K.; Jiang, X.; Zhang, Y.; Shu, H. B.; Gao, P.; Liu, L.; Wang, X. Y. Synchronous tailoring surface structure and chemical composition of Li-rich-layered oxide for high-energy lithium-ion batteries. *Adv. Funct. Mater.* **2018**, *28*, 1803392.

[29] Chen, J.; Zou, G. Q.; Deng, W. T.; Huang, Z. D.; Gao, X.; Liu, C.; Yin, S. Y.; Liu, H. Q.; Deng, X. L.; Tian, Y. et al. Pseudo-bonding and electric-field harmony for Li-rich Mn-based oxide cathode. *Adv. Funct. Mater.* **2020**, *30*, 2004302.

[30] Lan, X. W.; Li, Y. Q.; Guo, S. T.; Yu, L.; Xin, Y.; Liu, Z. F.; Hu, X. L. Stabilizing Li-rich layered cathode materials by nanolayer-confined crystal growth for Li-ion batteries. *Electrochim. Acta* **2020**, *333*, 135466.

[31] Yu, R. Z.; Zhang, Z. J.; Jamil, S.; Chen, J. C.; Zhang, X. H.; Wang, X. Y.; Yang, Z. H.; Shu, H. B.; Yang, X. K. Effects of nanofiber architecture and antimony doping on the performance of lithium-rich layered oxides: Enhancing lithium diffusivity and lattice oxygen

stability. *ACS Appl. Mater. Interfaces* **2018**, *10*, 16561–16571.

[32] Hu, S. J.; Li, Y.; Chen, Y. H.; Peng, J. M.; Zhou, T. F.; Pang, W. K.; Didier, C.; Peterson, V. K.; Wang, H. Q.; Li, Q. Y. et al. Insight of a phase compatible surface coating for long-durable Li-rich layered oxide cathode. *Adv. Energy Mater.* **2019**, *9*, 1901795.

[33] Zhang, C. X.; Wei, B.; Wang, M. Y.; Zhang, D. T.; Uchiyama, T.; Liang, C. P.; Chen, L. B.; Uchimoto, Y.; Zhang, R. F.; Wang, P. et al. Regulating oxygen covalent electron localization to enhance anionic redox reversibility of lithium-rich layered oxide cathodes. *Energy Storage Mater.* **2022**, *46*, 512–522.

[34] Karuppasamy, K.; Rabani, I.; Vikraman, D.; Bathula, C.; Theerthagiri, J.; Bose, R.; Yim, C. J.; Kathalingam, A.; Seo, Y. S.; Kim, H. S. ZIF-8 templated assembly of La3+-anchored ZnO distorted nano-hexagons as an efficient active photocatalyst for the detoxification of rhodamine B in water. Environ. *Pollut.* **2021**, *272*, 116018.

[35] Ding, X. K.; Luo, D.; Cui, J. X.; Xie, H. X.; Ren, Q. Q.; Lin, Z. An ultra-long-life lithium-rich Li1.2Mn0.6Ni0.2O2 cathode by three-in-one surface modification for lithium-ion batteries. *Angew. Chem., Int. Ed.* **2020**, *59*, 7778–7782.

[36] Lei, Y. K.; Elias, Y.; Han, Y. K.; Xiao, D. D.; Lu, J.; Ni, J.; Zhang, Y. C.; Zhang, C. M.; Aurbach, D.; Xiao, Q. F. Mitigation of oxygen evolution and phase transition of Li-rich Mn-based layered oxide cathodes by coating with oxygen-deficient perovskite compounds. *ACS Appl. Mater. Interfaces* **2022**, *14*, 49709–49718.

[37] Cui, S. L.; Zhang, X.; Wu, X. W.; Liu, S.; Zhou, Z.; Li, G. R.; Gao, X. P. Understanding the structure–performance relationship of lithium-rich cathode materials from an oxygen-vacancy perspective. *ACS Appl. Mater. Interfaces* **2020**, *12*, 47655–47666.

[38] Yu, Y.; Yang, Z.; Zhong, J. J.; Liu, Y. Y.; Li, J. L.; Wang, X. D.; Kang, F. Y. A simple dual-ion doping method for stabilizing Li-rich materials and suppressing voltage decay. *ACS Appl. Mater. Interfaces* **2020**, *12*, 13996–14004.

[39] Huang, C.; Wang, Z. J.; Fang, Z. Q.; Zhao, S. X.; Ci, L. J. Achieving high initial Coulombic efficiency and low voltage dropping in Li-rich Mn-based cathode materials by metal-organic frameworks-derived coating. *J. Power Sources* **2021**, *499*, 229967.

[40] Huang, C.; Fang, Z. Q.; Wang, Z. J.; Zhao, J. W.; Zhao, S. X.; Ci, L. J. Accelerating the activation of Li2MnO3 in Li-rich high-Mn cathodes to improve its electrochemical performance. *Nanoscale* **2021**, *13*, 4921–4930.

[41] Liu, Q.; Su, X.; Lei, D.; Qin, Y.; Wen, J. G.; Guo, F. M.; Wu, Y. A.; Rong, Y. C.; Kou, R. H.; Xiao, X. H. et al. Approaching the capacity limit of lithium cobalt oxide in lithium ion batteries via lanthanum and aluminium doping. *Nat. Energy* **2018**, *3*, 936–943.

[42] Ku, L.; Cai, Y. X.; Ma, Y. T.; Zheng, H. F.; Liu, P. F.; Qiao, Z. S.; Xie, Q. S.; Wang, L. S.; Peng, D. L. Enhanced electrochemical performances of layered-spinel heterostructured lithium-rich Li1.2Ni0.13Co0.13Mn0.54O2 cathode materials. *Chem. Eng. J.* **2019**, *370*, 499–507.

[43] Zuo, C. J.; Hu, Z. X.; Qi, R.; Liu, J. J.; Li, Z. B.; Lu, J. L.; Dong, C.; Yang, K.; Huang, W. Y.; Chen, C. et al. Double the capacity of manganese spinel for lithium-ion storage by suppression of cooperative Jahn–Teller distortion. *Adv. Energy Mater.* **2020**, *10*, 2000363.

[44] Fu, C. C.; Wang, J. Y.; Wang, J. F.; Meng, L. L.; Zhang, W. M.; Li, X. T.; Li, L. P. A LiPF6-electrolyte-solvothermal route for the synthesis of LiF/LixPFyOz-coated Li-Rich cathode materials with enhanced cycling stability. *J. Mater. Chem. A* **2019**, *7*, 23149–23161.